Article

Metal Oxide Quantum Dots Embedded in Silica Matrices Made by Flame Spray Pyrolysis

Keroles B. Riad, Suong V. Hoa, and Paula M. Wood-Adams*

Read Online

ACCESS | Metrics & More | Article Recommendations | SI Supporting Information

ABSTRACT: Quantum dots have unique size-dependent properties and promising applications. However, their use in many applications remains hindered by mechanical, thermal, and chemical instability and the lack of viable quantum dot mass-production processes. Embedding quantum dots in matrices such as silica counteracts the instability challenges in some applications while preserving their unique properties and applicability. Here, we synthesize quantum dots of four different metal oxides embedded in a silica matrix in a one-step mass-production process using flame spray pyrolysis.

1. INTRODUCTION

Quantum dots are the object of considerable interest because of their remarkable optical and electronic properties such as high quantum efficiency, narrow size-dependent absorption, and luminescence windows.[1−3] The quantized effect[4] is most easily observed when the crystal size is below the Bohr diameter.[3] The applications of metal oxide quantum dots range from photocatalysis (TiO_2),[5−7] ultraviolet (UV) protection films (ZnO),[8,9] gas sensing (SnO_2),[10,11] to high-temperature superconductors (CuO).[12] Further, semiconducting quantum dots have been shown to photopolymerize acrylics via free-radical polymerization.[13−15] We have recently shown that semiconducting nanoparticles such as TiO_2 and ZnO can photopolymerize epoxy via cationic polymerization.[16] The two most major obstacles faced by quantum dots preventing the commercialization of many of these applications are their mechanical, thermal, and chemical instability and the lack of viable large-scale production.[17−19]

The stability of quantum dots can be improved by embedding them in amorphous matrices.[18] For example, embedding quantum dots in an amorphous carbon matrix counteracts the aggregation and volume swelling challenges encountered during lithiation in battery applications.[17] Ge et al.[20] also embedded CuO quantum dots (1−2 nm) in a silica matrix, which showed improved thermal stability. Further, these amorphous matrices improve wetting and dispersion that are critical to photocatalytic activity.[21]

The synthesis of quantum dots embedded in amorphous matrices suffers from the inherent challenge of high activation energy because of the composition and solubility of the semiconducting particles in the amorphous matrix.[18] Further, quantum dots embedded in amorphous matrices intended for photocatalytic applications must avoid a core−shell structure where the semiconducting material core is hermetically sealed by the amorphous shell, as this will eliminate surface reactions.[22] However, segregated particles with distinct crystalline and amorphous domains exhibit high photocatalytic activity.[22]

The need for viable high-volume production of quantum dots remains unmet. Quantum dots are usually synthesized using wet chemistry techniques that are relatively complex, require hours, and are with a production rate in the order of grams per day.[5,9,17,18,23,24] Alternatively, flame spray pyrolysis (FSP) is a one-step process that produces metal oxide nanoparticles at industrial rates in the order of tons per day.[25] FSP also allows great versatility in combining different materials. Various FSP process parameters can be used to control particle size such as the dispersion gas and/or precursor flow rates.[26] However, precise control of the very small crystal size required to synthesize quantum dots remains elusive. Teleki and Pratsinis[27] observed the blue shift in band gap energy that is characteristic of the quantized effect in titania that is thermophoretically collected at different heights from within the flame. To the best of our knowledge, there is currently only one publication on synthesizing ZnO particles small enough to exhibit the quantized effect via FSP.[28] In that study, Mädler et al. added silica to the precursor mixture to provide a matrix that caps the size of ZnO crystals and provides access to the smaller crystal size and narrower size distribution that exists at early stages within the flame. The coprecipitation of ZnO and silica hinders the sintering of ZnO or its coalescence. Further, Tani et al.[29] demonstrated the thermal stability of flame-made ZnO/SiO_2 particles. Here, this approach is generalized as we demonstrate that FSP can be used to synthesize quantum dots, embedded in a silica matrix, of many metal oxide semiconducting materials: TiO_2, ZnO
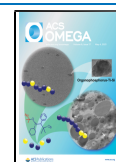
(over a broader size range than what Mädler et al. explored), SnO_2, and CuO.

2. THEORY

The exciton Bohr diameter of a semiconducting material, d_{Bohr}, is calculated via eq 1.[30,31]

$$d_{Bohr} = 2R_{Bohr} = \frac{2\hbar^2\varepsilon}{e^2\mu} \qquad (1)$$

where $\hbar = 1.05 \times 10^{-34}$ J s is the reduced Plank's constant, ε is the dielectric constant of the material, $e = 1.6 \times 10^{-19}$ C is the elementary charge, and μ is the reduced mass of the material's exciton.

Equation 2 governs the relationship between the crystal size in terms of radius and band gap energy (E^*).[9]

$$E^* = E_g + \frac{\hbar^2\pi^2}{2R^2\mu} - \frac{1.8e^2}{\varepsilon R} \qquad (2)$$

where E_g is the bulk band gap energy of the material (at $R \rightarrow \infty$). Equation 2 illustrates that the quantized effect is most significant at sizes below the exciton Bohr diameter but still occurs at bigger sizes. It is important to note that eq 2 has limitations because of the assumptions it involves,[18,32] particularly at sizes below 3 nm, because of a significant increase in the electrons' kinetic energy.[33]

Table 1. Material Properties

	TiO_2 (Anatase)[5]	ZnO (Zincite)	SnO_2 (Cassiterite)[34]	CuO (Monoclinic)
ε	31	3.7[9]	14	25[35]
μ/m_0	1.630	0.157[36]	0.275	0.381[37]
Eg (eV)	3.2	3.2[36]	3.6	1.5[37]
Bohr diameter (nm) from literature	2	2.5[36]	5.4	6.6–28.7[23]
calculated Bohr diameter (nm) (eq 2)	2	2.5	5.4	7

Table 1 shows the standard properties of each of the materials used in this study, where $m_0 = 9.1 \times 10^{-31}$ kg is the mass of a free electron. The exciton Bohr diameter calculated using eq 1 and the tabulated material properties are consistent with the values found in the literature.

3. RESULTS AND DISCUSSION

Figure 1 shows the X-ray powder diffraction (XRD) patterns of flame-made TiO_2, ZnO, SnO_2, and CuO, where X is the molar fraction of the metal oxide and the balance are silica. Therefore, when "X" is 1, the particles are made of pure metal oxide and contain no silica. However, particles contain silica when "X" is smaller than 1. The XRD patterns indicate that ZnO, SnO_2, and CuO have hexagonal, tetragonal, and monoclinic crystal structures, respectively. TiO_2 has anatase (reflection at 25°) and monoclinic (weak reflection at 15°) crystal structures, consistent with our earlier observations,[26] and traces of rutile (reflection at 30°). The XRD patterns of flame-made TiO_2 with X = 1, 0.8, and 0.7 can be used to reliably calculate the average crystal size, d(XRD) (Table 2), which are found to be 5.8, 3.3, and 2.3 nm, respectively. The
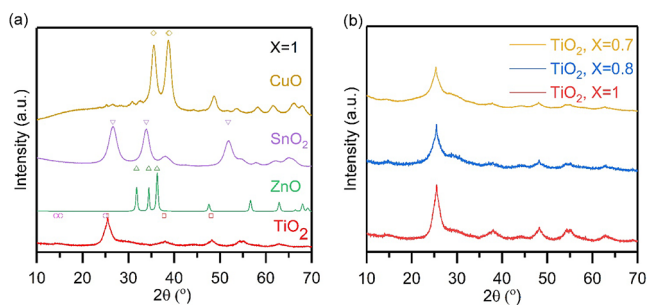

Figure 1. XRD patterns of flame-made particles: (a) TiO_2, CuO, SnO_2, and ZnO (X = 1) and (b) TiO_2 (X = 1, 0.8, and 0.7). The positions of the most important reflections in standard ICDD XRD patterns of TiO_2 (anatase, PDF card 00-021-1272, squares), TiO_2 (monoclinic, PDF Card 00-46-1238, circles), ZnO (hexagonal, PDF card 00-036-1451, upside triangles), SnO_2 (tetragonal, PDF card 00-041-1445, downside triangles), and CuO (monoclinic, PDF card 00-045-0937, diamonds) are indicated.

TiO_2 average crystal size, d(XRD), decreases as the silica loading increases (X decreases). Similarly, the XRD patterns of ZnO, SnO_2, and CuO can be used to reliably calculate average crystal size, d(XRD), only when X = 1. Figure S1 shows the XRD patterns of particles with X = 0.7, demonstrating that the very small crystal sizes, which significantly broaden XRD reflections, and the presence of amorphous silica render calculations of the average crystal size, d(XRD), for all other flame-made particles considered here unreliable. This challenge was previously encountered by Tani et al. in similar flame-made ZnO/SiO_2 particles.[29] The average crystal size, d(XRD), of flame-made TiO_2, ZnO, SnO_2, and CuO (X = 1) are 5.8, 28.6, 4.8, and 7.4 nm, respectively. The average crystal size, d(XRD), of SnO_2 (X = 1), 4.8 nm, is smaller than the exciton Bohr diameter of 5.4 nm.

Table 2 also shows the Brunauer–Emmett–Teller (BET)-equivalent particle size, d(BET), calculated from SSA measurements (Table S1) via eq 3. The average particle size, d(BET), is generally comparable to the average crystal size, d(XRD), if not slightly bigger because of the presence of amorphous silica. ZnO is the only exception perhaps because the flame-made ZnO particles have a rodlike shape[38] (Figure S2), while (BET) calculations from SSA assume spherical particles (eq 3). As the silica content increases (X decreases), the average particle size, d(BET), decreases to a minimum, levels off, and then starts increasing. The presence of such minima has been previously observed in flame-made ZnO quantum dots.[28] The average particle sizes, d(BET), of SnO_2 (X = 0.7, 0.5, and 0.3) and CuO (X = 0.7, 0.5, and 0.3) are smaller than their exciton Bohr diameters of 5.4 and 7 nm, respectively. Since the overall particle sizes in these cases are smaller than the Bohr diameters, certainly the crystal sizes are also smaller than the Bohr diameters.

Figure 2 shows HR-transmission electron microscopy (TEM) images of flame-made (a) TiO_2, (b) ZnO, (c) SnO_2, and (d) CuO with X = 0.7. Figure 2a shows the lattice spacing of both anatase (0.3 nm) and monoclinic (0.6 nm) TiO_2 crystal structures consistent with our earlier observations.[26] Figure 2b shows the lattice spacing of a hexagonal (0.27 nm) ZnO crystal structure. Further, Figures 2b and S3 show the rodlike shape of ZnO mentioned earlier. Figure 2c shows the lattice spacing of a tetragonal (0.34 and 0.27 nm) SnO_2 crystal structure. Figure 2d shows the lattice spacing of a monoclinic (0.26 nm) CuO crystal structure. All observed lattice spacings

Table 2. Size and Band Gap Energy

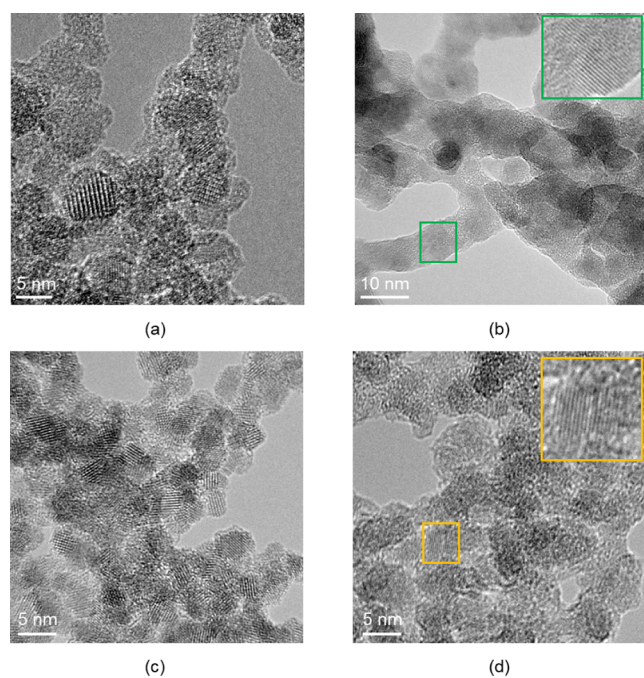| material	d(Bohr) (nm)	X	crystal and particle sizes (nm)			band gap energy (eV)	
			d(XRD)	d(BET)	d(UV−vis)	calculated	measured
TiO$_2$	2	1	5.8	5.5	2.1	3.2	3.4
		0.8	3.3	5.5	2.1	3.3	3.4
		0.7	2.3	5.6	1.7	3.4	3.5
		0.1		9.0	0.9		4.3
ZnO	2.34	1	28.6	42.0	bulk	3.2	3.2
		0.8		7.1	8.2		3.4
		0.7		7.8	6.9		3.4
		0.3		4.8	4.3		3.7
		0.1		4.2	2.1		5.4
SnO$_2$	5.4	1	4.8	5.4	5.2	3.8	3.8
		0.7		4.7	4.0		3.9
		0.5		4.9	3.7		4.0
		0.3		4.9	3.0		4.2
		0.2		5.6	2.7		4.3
		0.1		6.4	2.2		4.7
CuO	7	1	7.4	8.9	4.5	1.6	1.7
		0.9		7.8	3.3		1.9
		0.7		5.5	1.8		2.7
		0.5		5.5	1.7		2.9
		0.3		6.1	1.6		3.0
		0.2		9.6	1.6		3.0
		0.1		10.3	1.4		3.5
		0.05		14.3	1.4		3.7

Figure 2. HR-TEM of (a) TiO$_2$, (b) ZnO, (c) SnO$_2$, and (d) CuO flame-made particles ($X = 0.7$). Insets in b and d are magnifications of observed crystal structures.

are consistent with the XRD patterns (Figure 1). We can observe that in all cases, crystals are between 2 and 5 nm in diameter, even though it is difficult to objectively quantify crystal size using imaging techniques. Most importantly, the HR-TEM images do not show outlier large particles normally observed in the case of broad size distributions. Further, we do not observe a silica coating that would be present in a core−shell structure. Instead, we observe distinct amorphous and

crystalline domains indicating segregated particles, consistent with Teleki's[22] observations of similar metal oxide/silica particles made using a co-mixing FSP process.

Figure 3 shows solid-state UV−vis spectra of TiO$_2$, ZnO, SnO$_2$, and CuO flame-made particles with various silica loading. The sudden drop that appears around 3.52 eV is an instrument artifact because of a lamp change. In all cases, as the silica loading increases (X decreases), the absorption onset shifts to higher energy. This blue shift is consistent with the effect because of the quantum confinement predicted by eq 2 that becomes observable as the crystal size approaches the exciton Bohr diameter calculated in Table 1. It is also important to note that it would be impossible to observe this quantized effect if the particle size distribution were too broad.[5] The inset in Figure 3d shows a photograph of flame-made CuO with various silica loading, demonstrating that their absorption is in the visible region. Note that the color of the flame-made CuO particles changes from dark red in the case of CuO ($X = 1$), to green in the case of CuO ($X = 0.7$), to blue in the case of CuO ($X = 0.1$), and to almost white in the case of CuO ($X = 0.05$). Finally, we observe repeatable anomalous peaks in the spectra of CuO ($X = 0.5$ and 0.3) between 2 and 2.5 eV, but we are unable to determine their source.

Table 2 shows the measured and theoretical band gap energies (E^*) of the synthesized particles. The band gap energies were measured using the exponential region of the absorption edge, as described in the literature using UV−vis Tauc plots (Figure 3).[39] The theoretical band gap energy is calculated via eq 2 using the average crystal size, d(XRD) (Table 2), when XRD is reliable. The theoretical and measured band gap energies are close, with less than 6% (max 0.2 eV) difference for all flame-made particles without silica ($X = 1$). Further, the measured band gap energies of flame-made TiO$_2$ with $X = 0.8$ and 0.7 are also consistent with the theoretical values and exhibit a quantized effect (3% error, 0.1 eV
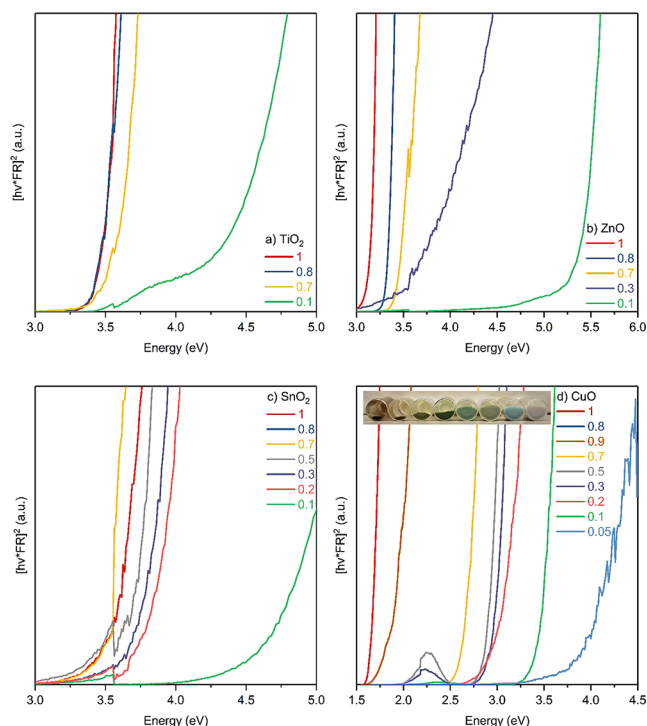
Figure 3. Solid-state UV−vis Tauc plots of flame-made metal oxide semiconducting nanoparticles. (a) TiO$_2$, (b) ZnO, (c) SnO$_2$, and (d) CuO (inset: photograph showing the color of the CuO particles, courtesy of Andrew Kingsley Jeyaraj—Copyright 2020). Figure shows a blue shift in band gap energy as silica loading increases and X decreases.
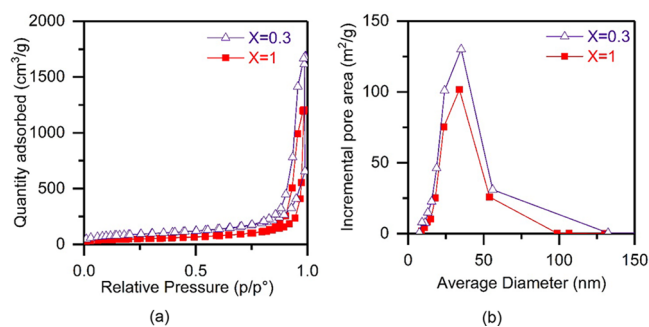

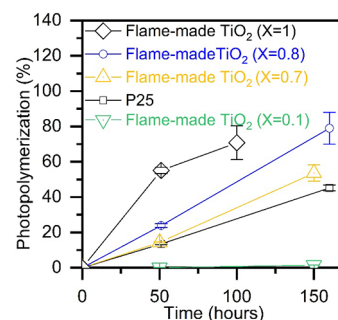**Figure 4.** SnO$_2$ (X = 1 and 0.3): (a) full isotherms and (b) pore size distribution.

Figure 5. Photocatalytic activity of epoxy photopolymerization by flame-made TiO$_2$ (X = 0.8, 0.7, and 0.1) compared with commercial P25 TiO$_2$. Error bars are 90% confidence intervals (n = 6).

difference). In all cases, as the silica loading increases (X decreases), the measured band gap energy increases to higher values consistent with the quantized effect predicted by eq 2.

Table 2 shows the back-calculated crystal size, d(UV−vis), associated with the measured band gap energy determined via eq 2. The crystal size, d(UV−vis), is smaller than the average particle size, d(BET), in most cases. This is because of the presence of the silica matrix. In one case, d(UV−vis) is larger than average particle size, d(BET). In addition to the experimental uncertainty, this discrepancy is because d(UV−vis) uses onset absorption stemming from the larger crystals,[28] while d(BET) is an average size.[40] In all cases, d(UV−vis) decreases as silica loading increases (X decreases). The crystal sizes, d(UV−vis), of flame-made TiO$_2$ (X = 0.7 and 0.1), ZnO (X = 0.1), SnO$_2$ (X = 0.7. 0.5, 0.3, 0.2, and 0.1), and CuO (all) are smaller than their respective exciton Bohr diameters (2, 2.34, 5.4, and 7 nm).

Porosity is an important factor affecting the particles' ability to catalyze surface reactions. Full adsorption BET isotherms are collected for flame-made SnO$_2$ (X = 1 and 0.3), which is plotted in Figure 4a. The pore size distribution (Figure 4b) indicates that most of the pores fall within the 25−50 nm range. This pore size range is much larger than the particle size, d(BET), as well as HR-TEM observations (Figure 2). This indicates that the pores are intraparticle as a result of the aggregation that takes place in the flame. Similar flame-made particles of a catalytic material embedded in a ceramic matrix have been observed to exhibit high catalytic activity because the intraparticle pores provide direct access to the catalyst.[41]

Figure 5 shows the epoxy photopolymerization[16] rate initiated by flame-made TiO$_2$ (X = 1, 0.8, 0.7, and 0.1) and commercial P25. Flame-made TiO$_2$ (X = 1) shows superior photocatalytic performance as compared to commercial P25 titania, the gold standard for photocatalysis.[26] The silica matrix in flame-made TiO$_2$ (X = 0.8 and 0.7) quantum dots slows the reaction but does not prohibit it, indicating that the silica matrix does not hermetically seal the semiconducting material surface. The epoxy photocuring reaction catalyzed by flame-made TiO$_2$ quantum dots (X = 0.8 and 0.7) is faster than that catalyzed by P25. The superior performance of the flame-made TiO$_2$ quantum dots, whether or not they are embedded in a silica matrix, can be attributed to factors including its high surface area (relative to 50 m^2/g in P25 TiO$_2$), the presence of the monoclinic crystal structure,[26] and improved wetting and dispersion because of the silica matrix.[21] However, the decreasing reaction rate as the silica loading increases (X decreases) can be attributed to the increase in the band gap energy of the particles (Table 2 and Figure 3) beyond the energy of light emitted by the UVA source in these photocuring experiments, as well as the decrease in the effective mass of TiO$_2$. This practically eliminates the reaction when catalyzed by TiO$_2$ (X = 0.1), despite the very large surface area of 282 m^2/g.

4. CONCLUSIONS

We synthesized via flame silica-embedded metal oxide quantum dots of TiO$_2$, ZnO, SnO$_2$, and CuO, showing that quantum dots of any band gap energy between the dark red side of the visible spectrum to the UVC region can be synthesized by FSP by choosing the appropriate metal oxide material and the silica content. Silica encapsulation enables the use of these quantum dots in various applications requiring higher mechanical, thermal, and/or chemical stability than what is afforded by the matrix-free quantum dots. The silica

matrix of the flame-made metal oxide quantum dots does not hermetically seal the particles, allowing particle–surface photocatalytic reactions to take place. Most significantly, the FSP synthesis process allows the mass production of those silica-embedded metal oxide quantum dots at an industrial scale ready for application.

5. EXPERIMENTAL SECTION

5.1. Particle Synthesis. A solution with 0.25 mol/L total metal concentration is prepared by diluting precursors with xylenes (Sigma-Aldrich, Reagent grade). The precursors used are titanium (IV) tetraisopropoxide (Sigma-Aldrich, 97%), Zn-2-ethylhexanoate (Strem Materials, 80%), tin-2-ethylhexanoate (Sigma-Aldrich, 92.5−100%), copper-2-ethylhexanoate (Strem Materials, 16−19% Cu), and hexamethyldisiloxane (Sigma-Aldrich, 98.5%) for Ti, Zn, Sn, Cu, and Si elements, respectively. This solution is fed at 1 mL/min through the capillary of the FSP reactor and atomized by 3.75 L/min of oxygen. The precursor spray is ignited with a pilot flame fueled by 1.25 L/min of CH_4 premixed with 2.5 L/min of O_2. Product nanoparticles are collected on glass fiber filters (Albet-Hahnemühle, GF 6, 25.7 cm diameter) placed in a water-cooled stainless-steel holder with the help of a vacuum pump (Busch, Seco SV 1040 C). Scheme 1 depicts the flame synthesis process.

Scheme 1. FSP Synthesis Process
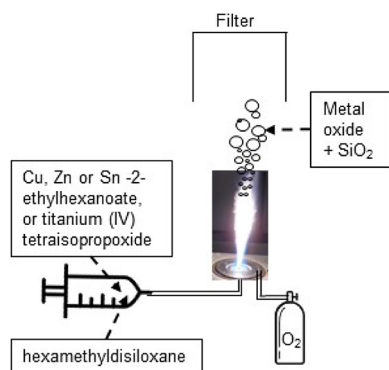
5.2. Characterization. XRD is performed on a Bruker D8 Advanced diffractometer (Cu Kα radiation, 40 kV, 30 mA, Bragg−Brentano geometry, equipped with a Lynxeye detector, 0.02° step size, 2 s/step) in the range of 10° < 2θ < 70°. The average crystal size, d(XRD), is calculated using the Rietveld method.[42]

Specific surface areas are determined by nitrogen adsorption (Micromeritics TriStar II) at 77 K, employing the BET isotherm after degassing the sample in nitrogen at 150 °C for at least 2 h. The average particle size, d(BET), in nanometer, is calculated using eq 3 from the specific surface area measurements using nitrogen adsorption.

$$d(\text{BET}) = \frac{6000}{\text{SSA} \times \rho} \quad (3)$$

where SSA is the specific surface area in m^2/g, and ρ is density in g/cm^3. Our flame-made particles are composites of metal oxides in silica matrix, and therefore, eq 4 is used to calculate their densities (ρ).

$$\rho_{\text{composite}} = X \times \rho_{\text{metal oxide}} + (1 - X) \times \rho_{\text{silica}} \quad (4)$$

The densities[43] of TiO_2 (anatase), ZnO (zincite), SnO_2 (cassiterite), CuO (monoclinic), and silica are as follows: 3.79,[44] 5.61, 6.85, 6.31, and 2.2 g/cm^3, respectively.

For porosity-related measurements, a Tristar 3000 is used to record the full adsorption isotherm of the as-prepared powder. The desorption isotherm is used to determine the pore size distribution.

Solid-state UV−vis spectra are measured using a Varian Cary 500 UV−vis spectrophotometer equipped with an integrating sphere using samples diluted 10 times with barium sulfate (Sigma-Aldrich, 99.99%).

TEM images with bright field is performed using a JEOL 2100 F FEG-TEM operated at 200 kV. Images are recorded with a Gatan Ultrascan 1000 camera.

X-ray photoelectron spectroscopy (XPS) spectra are collected using a K-Alpha Thermo Scientific spectrometer with an Al Kα, 1486.6 eV source. An X-ray beam size with Φ400 μm is used, and three points are measured on the sample surface. To minimize the effect of possible charge on the sample surface, the flood gun-generated low-energy electrons (plus Ar+ ion) are utilized to compensate charging. The survey scanning to provide the information of element percentage (atom %) for all possible atoms on the sample surface is set up at a full energy scale, pass energy of 200 eV, scanning step size of 1 eV, dwell time of 50 μs, and is an average of three scans. The high-resolution scanning to provide the chemical state (bond) information for individual elements C, O, and Cu is set up at a specific energy scale (C 1s: 274.5−298.5 eV; O 1s: 524.8−544.8 eV; Cu 2p: 920−970 eV), pass energy of 50 eV, scanning step size of 0.1 eV, dwell time of 50 μs, and is an average of 10 scans.

Figure S3 shows XPS spectra of flame-made copper oxide (X = 1, 0.7, and 0.1). Peaks at binding energies of 940−945 and 965 eV exist in CuO but not Cu_2O.[45] Thus, these XPS spectra confirm that the CuO oxidation state is dominant in our flame-made copper oxide whether silica is used or not.

5.3. Photocatalytic Activity. Mixtures (1.5 g total weight) consisting of 1,4-cyclohexanedimethanol diglycidyl ether (Sigma-Aldrich, technical grade), 10 wt % 1-phenylethanol (Sigma-Aldrich, 99.5%), and 5 wt % nanoparticles are stirred overnight and then sonicated for 30 min, while being water-cooled (5 s on, 20 s off for a total time of 40 min, 95% amplitude, 40 W, 100 000 J total energy) using a Vibracell VCX 500 equipped with a cup horn. Mixtures are prepared using commercial titania P25 (Evonik) or flame-made TiO_2 (X = 0.8). The mixtures are blade coated on microscope glass slides using 0.0025-in.-thick Kapton tape (McMaster-Carr). These films are radiated using a 365 nm UVA lamp (UVP, XX-15 M), with a light intensity of approximately 2 mW/cm^2 at the surface of the films. The cure percentage is measured by Fourier transform infrared spectroscopy in the ATR mode on six different spots of each film using 64 scans at 1 cm^{-1} resolution scanning from 600 to 4000 cm^{-1} (Bruker Vertex 70v). Additional details have been published previously.[16]

■ ASSOCIATED CONTENT

ⓢ Supporting Information

The Supporting Information is available free of charge at https://pubs.acs.org/doi/10.1021/acsomega.0c06227.

XRD patterns of flame-made particles (X = 0.7) (Figure S1); HR-TEM of ZnO (X = 0.7) (Figure S2); XPS

spectra of flame-made CuO (X = 1 and 0.7) (Figure S3); BET-specific surface area (Table S1) (PDF)

■ AUTHOR INFORMATION

Corresponding Author

Paula M. Wood-Adams − *Laboratory for the Physics of Advanced Materials, Department of Chemical and Material Engineering, Concordia University, Montreal, Quebec H3G 2J2, Canada;* ◉ orcid.org/0000-0003-1562-3924; Email: paula.wood-adams@concordia.ca

Authors

Keroles B. Riad − *Laboratory for the Physics of Advanced Materials, Department of Chemical and Material Engineering, Concordia University, Montreal, Quebec H3G 2J2, Canada;* ◉ orcid.org/0000-0002-2739-1000

Suong V. Hoa − *Concordia Center for Composites, Department of Mechanical, Industrial and Aerospace Engineering, Concordia University, Montreal, Quebec H3G 2J2, Canada*

Complete contact information is available at:
https://pubs.acs.org/10.1021/acsomega.0c06227

Author Contributions

The manuscript was written through contributions of all authors. All authors have given approval to the final version of the manuscript.

Notes

The authors declare no competing financial interest.

■ REFERENCES

(1) Kamat, P. V.; Scholes, G. D. Quantum dots continue to shine brightly. *J. Phys. Chem. Lett.* **2016**, *7*, 584−585.

(2) Bera, D.; Qian, L.; Tseng, T.; Holloway, P. H. Quantum dots and their multimodal application: A review. *Materials* **2010**, *3*, 2260−2345.

(3) Alivisatos, A. P. Semiconductor clusters, nanocrystals, and quantum dos. *Science* **1996**, *271*, 933−937.

(4) Ekimov, A. I.; Onuschenko, A. A. Quantum size effect in three-dimensional microscopic semiconductor crystals. *J. Exp. Theor. Phys.* **1981**, *34*, 345−349.

(5) Satoh, N.; Nakashima, T.; Kamikura, K.; Yamamoto, K. Quantum size effect in TiO$_2$ nanoparticles prepared by finely controlled metal assembly on dendrimer templates. *Nat. Nanotechnol.* **2008**, *3*, 106−111.

(6) Fujishima, A.; Honda, K. Electrochemical photolysis of water at a semiconductor electrode. *Nature* **1972**, *238*, 37−38.

(7) O'Regan, B.; Grätzel, M. A Low-cost, high-efficiency solar cell based on dye-sensitized colloidal TiO$_2$ films. *Nature* **1991**, *353*, 737−740.

(8) Meulenkamp, E. Synthesis and growth of ZnO nanoparticles. *J. Phys. Chem. B* **1998**, *102*, 5566−5572.

(9) Lin, K. F.; Cheng, H. M.; Hsu, H. C.; Lin, L. J.; Hsieh, W. F. Band gap variation of size-controlled ZnO quantum dots synthesized by sol-gel method. *Chem. Phys. Lett.* **2005**, *409*, 208−211.

(10) Wan, Q.; Huang, J.; Xie, Z.; Wang, T.; Dattoli, E.; Lu, W. Branched SnO$_2$ nanowires on metallic nanowire backbones for ethanol sensors application. *Appl. Phys. Lett.* **2008**, *92*, No. 102101.

(11) Ma, J.; Zhang, J.; Wang, S.; Wang, Q.; Jiao, L.; Yang, J.; Duan, X.; Liu, Z.; Lian, J.; Zheng, W. Superior gas-sensing and lithium-storage performance SnO$_2$ nanocrystals synthesized by hydrothermal method. *CrystEngComm* **2011**, *13*, 6077−6081.

(12) Rehman, S.; Mumtaz, A.; Hasanain, S. Size effects on the magnetic and optical properties of CuO nanoparticles. *J. Nanopart. Res.* **2011**, *13*, 2497−2507.

(13) Hoffman, A.; Yee, H.; Mills, G.; Hoffmann, M. Photoinitiated polymerization of methyl methacrylate using Q-sized ZnO colloids. *J. Phys. Chem.* **1992**, *96*, 5540−5546.

(14) Stroyuk, A.; Granchak, V.; Korzhak, A.; Kuchmii, S. Photoinitiation of buthylmethacrylate polymerization by colloidal semiconductor nanoparticles. *J. Photochem. Photobiol. A* **2004**, *162*, 339−351.

(15) Zhang, J.; Huang, Y.; Jin, X.; Nazartchouk, A.; Liu, M.; Tong, X.; Jiang, Y.; Ni, L.; Sun, S.; Sang, Y.; Liu, H.; Razzari, L.; Vetrone, F.; Claverie, J. Plasmon enhanced upconverting core@trible-shell nano-particles as recyclable panchromatic initiators (blue to infrared) for radical polymerization. *Nanoscale Horiz.* **2019**, *4*, 907−917.

(16) Riad, K. B.; Arnold, A. A.; Claverie, J. P.; Hoa, S. V.; Wood-Adams, P. M. Photopolymerization using metal oxide semiconducting nanoparticles for epoxy-based coatings and patterned films. *ACS Appl. Nano Mater* **2020**, *3*, 2875−2880.

(17) Chen, D.; Huang, S.; Huang, R.; Zhang, Q.; Le, T.; Cheng, E.; Hu, Z.; Chen, Z. Highlights on advances in SnO$_2$ quantum dots: Insights into synthesis strategies, modifications and applications. *Mater. Res. Lett.* **2018**, *6*, 462−488.

(18) Xue, J.; Wang, X.; Jeong, J. H.; Yan, X. Fabrication, photoluminescence and applications of quantum dots embedded glass ceramics. *Chem. Eng.* **2020**, *383*, No. 123082.

(19) Leschkies, K. S.; Divakar, R.; Basu, J.; Enache-Pommer, E.; Boercker, J. E.; Carter, B. C.; Kortshagen, U. R.; Norris, D. J.; Aydil, E. S. Photosensitization of ZnO nanowires with CdSe quantum dots for photovoltaic devices. *Nano Lett.* **2007**, *7*, 1793−1798.

(20) Ge, Y.; Shah, Z. H.; Wang, C.; Wang, J.; Mao, W.; Zhang, S.; Lu, R. In situ encapsulation of ultrasmall CuO quantum dots with controlled band-gap and reversible thermochromism. *ACS Appl. NanoMat. Int.* **2015**, *7*, 26437−26444.

(21) Teleki, A.; Akhtar, M. K.; Pratsinis, S. E. The quality of SiO$_2$-coatings on flame-made TiO$_2$-based nanoparticles. *J. Mater. Chem.* **2008**, *18*, 3547−3555.

(22) Teleki, A.; Heine, M. C.; Krumeich, F.; Akhtar, M. K.; Pratsinis, S. E. In situ coating of flame-made TiO$_2$ particles with nanothin SiO$_2$ films. *Langmuir* **2008**, *24*, 12553−12558.

(23) Borgohain, K.; Mahamuni, S. Formation of single-phase CuO quantum particles. *J. Mater. Res.* **2002**, *17*, 1220−1223.

(24) Zhu, H.; Yang, D.; Yu, G.; Zhang, H.; Yao, K. A simple hydrothermal route for synthesizing SnO$_2$ quantum dots. *Nanotechnology* **2006**, *17*, No. 2386.

(25) Wegner, K.; Pratsinis, S. E. Scale-up of Nanoparticle Synthesis in Diffusion Flame Reactors. *Chem. Eng. Sci.* **2003**, *58*, 4581−4589.

(26) Riad, K. B.; Wood-Adams, P. M.; Wegner, K. Flame-made TiO$_2$(B). *Mater. Res. Bull.* **2018**, *106*, 276−281.

(27) Teleki, A.; Pratsinis, S. E. Blue nano titania made in diffusion flames. *Phys. Chem. Chem. Phys.* **2009**, *11*, 3742−3747.

(28) Mädler, L.; Stark, W.; Pratsinis, S. Rapid synthesis of stable ZnO quantum dots. *J. Appl. Phys.* **2002**, *92*, No. 6537.

(29) Tani, T.; Mädler, L.; Pratsinis, S. E. Synthesis of zinc oxide/silica composite nanoparticles by flame spray pyrolysis. *J. Mat. Sci.* **2002**, *37*, 4627−4632.

(30) Wang, Y.; Herron, N. Nanometer-sized semiconductor clusters: materials synthesis, quantum size effects, and photophysical properties. *J. Phys. Chem.* **1991**, *95*, 525−532.

(31) Knox, R. S. *Theory of Excitons*; Solid state physics supplement 5. Academic Press: New York, 1963.

(32) Alivisatos, A. P.; Harris, A. I.; Levinos, N. J.; Steigerwald, M. L.; Brus, L. E. Electronic states of semiconductor clusters: Homogeneous and inhomogeneous broadening of the optical spectrum. *J. Chem. Phys.* **1988**, *89*, No. 4001.

(33) Spanhel, L.; Anderson, M. A. Semiconductor Clusters in the sol-gel process: Quantized aggregation, gelation, and crystal growth in concentrated ZnO colloids. *J. Am. Chem. Soc.* **1991**, *113*, 2826−2833.

(34) Xu, X.; Zhuang, J.; Wang, X. SnO_2 quantum dots and quantum wires: Controllable synthesis, self-assembled 2D architectures, and gas-sensing properties. *J. Am. Chem. Soc.* **2008**, *130*, 12527−12535.

(35) Sarkar, S.; Jana, P. K.; Chaudhuri, B. K.; Sakata, H. Copper (II) oxide as a giant dielectric material. *Appl. Phys. Lett.* **2006**, *89*, No. 212905.

(36) Redmond, G.; O'Keeffe, A.; Burgess, C.; MacHale, C.; Fitzmaurice, D. Spectroscopic determination of the flatband potential of transparent nanocrystalline zinc oxide films. *J. Phys. Chem.* **1993**, *97*, 11081−11086.

(37) Parhizkar, M.; Singh, S.; Nayak, P. K.; Kumar, N.; Muthe, K. P.; Gupta, S. K.; Srinivasa, R. S.; Talwar, S. S.; Major, S. S. Nanocrystalline CuO films prepared by pyrolysis of Cu-arachidate LB multilayers. *Colloids Surf.* **2005**, *257−258*, 277−282.

(38) Hembram, K.; Sivaprakasam, D.; Rao, T.; Wegner, K. Large-scale manufacture of ZnO nanorods by flame spray pyrolysis. *J. Nanopart. Res.* **2013**, *15*, 1−11.

(39) Tauc, J. Absorption edge and internal electric fields in amorphous semiconductors. *Mat. Res. Bull.* **1970**, *5*, 721−729.

(40) Brunauer, S.; Emmett, P.; Teller, E. Adsorption of gases in multimolecular layers. *J. Am. Chem. Soc.* **1938**, *60*, 309−319.

(41) Strobel, R.; Stark, W. J.; Mädler, L.; Pratsinis, S. E.; Baiker, A. Flame-made platinum/alumina: structural properties and catalytic behavior in enantioselective hydrogenation. *J. Catal.* **2003**, *213*, 296−304.

(42) Cheary, R. W.; Coelho, A. A. Axial divergence in a conventional X-ray powder diffractometer. I. Theoretical Foundation. *J. Appl. Cryst.* **1998**, *31*, 851−861.

(43) Haynes, W. M. *CRC Handbook of Chemistry and Physics*; CRC press, 2014.

(44) Banfield, J. F.; Veblen, D. R. The identification of naturally occurring TiO_2 (B) by structure determination using high-resolution electron microscopy, image simulation, and distance-least-squares refinement. *Am. Mineral.* **1991**, *76*, 343−353.

(45) Jiang, R.; Prendergast, D.; Borondics, F.; Porsgaard, S.; Giovanetti, L.; Pach, E.; Newberg, J.; Bluhm, H.; Besenbacher, F.; Salmeron, M. Experimental and theoretical investigation of the electronic structure of Cu_2O and CuO thin films on Cu(110) using x-ray photoelectron and absorption spectroscopy. *J. Chem. Phys.* **2013**, *138*, No. 024704.